nature communications

Article

https://doi.org/10.1038/s41467-025-56227-9

Improved radicchio seedling growth under $CsPbI_3$ perovskite rooftop in a laboratory-scale greenhouse for Agrivoltaics application

Received: 22 May 2024

Accepted: 13 January 2025

Published online: 11 March 2025

Check for updates

Carlo Spampinato[1,2], Salvatore Valastro[1] ✉, Gaetano Calogero[1], Emanuele Smecca[1], Giovanni Mannino[1], Valentina Arena[1], Raffaella Balestrini[3,4] ✉, Fabiano Sillo[3], Lucio Ciná[5], Antonino La Magna[1] & Alessandra Alberti[1] ✉

Agrivoltaics, integrating photovoltaic systems with crop cultivation, demands semitransparent solar modules to mitigate soil shadowing. Perovskite Solar Cells (PSC) offer competitive efficiency, low fabrication costs, and high solar transmittance, making them suitable for agrivoltaic applications. However, the impact of PSC light filtering on plant growth and transcriptomics remains underexplored. This study investigates the viability and agronomic implications of the growth of radicchio seedlings (*Cichorium intybus* var. *latifolium*) in laboratory-scale greenhouses integrating Perovskites-coated rooftops. Eu-enriched $CsPbI_3$ layers are chosen to provide semi-transparency and phase stability while radicchio has limited size and grows in pots. Despite the reduced light exposure, radicchio seedlings exhibit faster growth and larger leaves than in the reference, benefiting from specific spectral filtering. RNA-sequencing reveals differential gene expression patterns reflecting adaptive responses to environmental changes. Simulations of full PSC integration demonstrate a positive energy balance in greenhouses to cover annual energy needs for lighting, irrigation, and air conditioning.

Agrivoltaics, by merging agriculture and renewable energy production, aims at efficient and sustainable farming activities in a self-consumption electrical scheme[1,2]. Traditional opaque photovoltaic (PV) silicon solar cells (SSC), with a record laboratory-scale efficiency of 26.88%[3] are currently used in open-field farms and greenhouses, providing plants with reduced temperature and protection from harsh weather. However, opaque SSC can hinder plant growth due to shading effects[4–6]. To address the problem of soil shadowing, semi-transparent (ST) PV modules are required[7]. ST PV technologies, such as organic (OSC), dye-sensitized (DSSC), and perovskite solar cells (PSC), offer semi-transparency and additional flexibility for coverages on bent surfaces. Among those possible choices, PSC offers versatility to regulate solar light transmittance. PSC are also competitive in terms of efficiency and fabrication costs[8,9]. As a matter of fact, PSC reached a current record efficiency of 26.7%, comparable to SSC while surpassing OSC (18.2%) and DSSC (13%)[10]. The estimated cost for a PSC is in the range of 0.22–0.25$Wp^{-1} [11], whilst OSC and DSSC cost is 0.23–0.34$Wp^{-1} and 0.5–0.94$Wp^{-1}, respectively[12].

However, PSC technology still faces significant challenges, particularly concerning long-term stability, scalability, and environmental impact. PSCs are prone to degradation over time due to the sensitivity of perovskite materials to moisture[13], heat, light exposure, and due to

[1]National Research Council - Institute for Microelectronics and Microsystems (CNR-IMM), Zona Industriale - Strada VIII no. 5, Catania 95121, Italy. [2]Dipartimento Scienze Matematiche e Informatiche, Scienze Fisiche e Scienze della Terra, Università Degli Studi di Messina, Viale Ferdinando Stagno d'Alcontres, 31, Messina 98166, Italy. [3]National Research Council (CNR), Institute for Sustainable Plant Protection, Strada delle Cacce, 73, Torino 10135, Italy. [4]National Research Council (CNR), Institute of Biosciences and Bioresources (IBBR), Street, Bari 70126, Italy. [5]Cicci Research s.r.l., Via Giordania, 227, Grosseto 58100, Italy. ✉e-mail: salvatore.valastro@cnr.it; raffaellamaria.balestrini@cnr.it; alessandra.alberti@cnr.it

weakness points at the interfaces with the charge transporting layers[14]. Additionally, the presence of lead in perovskite composition raises environmental concerns[15]. Efforts to address these issues have been developed including encapsulating materials to protect PSCs from environmental agents and to capture leaked lead eventually; while enhancing performance and materials stability is done through compositional and interface engineering[16,17].

In the literature, OSC and DSSC have been successfully applied in greenhouses for tomato[18–21] and lettuce growth[22], enabling photoconversion efficiency of 3–5%. Recent experiments have also highlighted the feasibility and the high potential of some kind of stable and efficient ST-PSC architectures for Agrivoltaics[8,23]. However, these studies lack information regarding how the integration of PSC impacts plant growth and its transcriptomics. Plants have different photoreceptors, and it is well known that light absorption by them typically triggers signal transduction pathways that alter gene expression and photomorphogenesis[24,25]. A core set of genes that responds to high light levels has been identified in plants, and these genes affect hormones, photosynthesis, and the phenylpropanoid pathway[26]. In the model plant *ARABIDOPSIS*, a genome-wide gene expression analysis identified 77 light-responsive genes dependent on photoreceptor cryptochrome 1 (*CRY1*) and 25 on a basic leucine zipper (*bZIP*) transcription factor (*HY5*). Moreover, in *cry1* and *hy5* deletion mutants, the regulation of early light-inducible proteins Elip1 and Elip2 was disrupted, with their induction being mediated by *CRY1* depending on blue light intensity[27]. The effects of other PV technologies on plant physiology and growth have been recently reported. It has been reported that smart glass films block approximately 9% of PAR in plants and more than half of the entire short-wave radiation[28]. This effect leads to impaired plant growth characterized by disrupted ion fluxes, increased leaf water loss, heightened sensitivity to the abscisic acid (ABA) stress hormone, and reduced stomatal pore sizes, impairing photosynthesis rates and overall plant growth[28]. On the other hand, it has been reported that shading, which might occurr under opaque PV panels, may induce the Shade Avoidance Syndrome (SAS) in plants, leading to morphological adaptations such as increased leaf area and altered chlorophyll content[29]. Metabolite profiles in plants can also change under shading, with polyphenol and carotenoid content variations. Shaded chicory plants (*Cichorium intybus* seedlings of cultivar "*Otrantina*") showed higher chicoric acid levels and lower chlorogenic acid levels compared to those grown under full sunlight[30]. On the other hand, reduced UV radiation has been shown to lower polyphenol content, while increased red light can enhance sucrose and hexose accumulation in *Lactuca sativa* and *C. intybus*[31].

In this paper, we investigate through a multidisciplinary approach the viability and the agronomic implications of growing radicchio seedlings, starting from their germinated seeds, in a laboratory-scale greenhouse under ST-perovskite-coated rooftop. Radicchio is a member of the chicory family renowned for its distinct bitter flavor and nutritional richness[32–34]. It is rich in molecules with high nutritional values such as anthocyanins, it is appreciated in international markets, and, thanks to its limited size, it is easy to grow in pots[35,36]. Radicchio can be cultivated both in open-field or greenhouses[37] depending on the specific preferences of the growers and the season. The germinated radicchio seeds are typically sowed in little buckets within greenhouses and exposed to the sun until the seedlings have enough grown[38]. In the usual agronomic procedures, the seedlings are subsequently transplanted into the soil of the greenhouse or in open field for the complete maturation of the plants[39]. Our investigation focuses on the initial stage of this process in laboratory-scale greenhouses, examining various replicates of seed germination and seedling growth under perovskite-filtered light for 15 days under a 12 LEDs tower acting as a solar simulator, compared to bare glass filtered light. The perovskite material used for the experiment is a fully inorganic perovskite, with composition $CsPbI_3$, which has demonstrated superior thermal stability compared to hybrid perovskites due to the lack of volatile components[40] and relatively high photo-conversion efficiency (record of 21.15%[41] achieved with bandgap values in the range 704–716 nm). These values allow a suitable tradeoff between light absorption (i.e., PSC photovoltaic efficiency) and transmittance for assuring semi-transparency to PSC devices. In comparison, narrower bandgap perovskites like $FAPbI_3$ (861 nm) and $MAPbI_3$ (775 nm), while achieving high-efficiency record[10,42,43], exhibit lower transparency in the visible range. Conversely, wider bandgap perovskites like $CsPbIBr_2$ (610 nm) offer higher transparency in the visible range but with a lower record efficiency[44]. In particular, we used Eu-enriched $CsPbI_3$ formulations[45,46] for the coverage of the laboratory rooftop, since it has been shown that the Eu improves quality and stability of the material by mitigating the formation of intrinsic defects and by increasing the surface-to-volume ratio of perovskite grains[9,47]. The effect of the perovskite-filtered light on radicchio seedlings was complementary assessed by RNA-sequencing analyses, shedding light on how metabolic and transcriptomics parameters of the seedlings are modified, entailing adaptive responses to environmental variations. Furthermore, simulations of PSC power production over time corroborated a positive balance between annual energy production and consumption in a large class of greenhouses by applying rooftops PSC integrating Eu-enriched $CsPbI_3$ for future technological scale-up.

Results

Structural and optical characterization of the perovskite film used as greenhouse rooftop

Light filtering by ST-PSC is expected to play a role in crop growth[48,49]. This is because the portion of the light spectrum called Photosynthetically Active Radiation (PAR)[50] laying in the range 400–700 nm[49] is used for photosynthesis. One approach to tailor PSC semi-transparency is reducing the thickness of the photoactive layer[17,51]. Hence, we have fabricated semitransparent $CsPbI_3$:EuI_2 perovskite layers by scaling down the thickness to 130 nm as measured by spectroscopic ellipsometry, through optimization of the spin-coating deposition parameters and perovskite precursor solution concentration. This thickness allows for a positive balance between transmittance (Average Transmittance 20–34%)[52] in the visible range and device power conversion efficiency (8–12%)[52]. In Supplementary Fig. 1, the best trade-off between efficiency and PAR average transmittance is shown. The perovskite-covered glasses were applied as schematically depicted in Fig. 1a to realize the greenhouse rooftops, that filter the incident light from the simulated sun before reaching the seedlings. We preliminary investigated the structural and optical characteristics of the perovskite layer to frame its behavior in the interaction with the incoming light.

The X-Ray diffraction (XRD) pattern in Fig. 1b shows prominent peaks at $2\theta = 14.4°$; $2\theta = 20.6°$; $2\theta = 28.9°$; $2\theta = 36°$, well featuring the orthorhombic γ -phase structure ascribed to the $CsPbI_3$ perovskite[53]. The narrow and well-defined perovskite peaks and the lack of contributions from the non-photoactive orthorhombic δ-phase (diagnostic peak expected at $2\theta = 9.8°$) prove the purity and the high crystalline quality of the fabricated perovskite layer[54–56]. The lattice parameters, obtained through a standard Rietveld refinement procedure, are presented in Supplementary Table 1. Eu-addition is used as a strategy to assure long-term stability to the perovskite layer[47]. Figure 1c shows the absorption coefficient (α) and the transmittance of the 130-nm-thick $CsPbI_3$:EuI_2 layer measured by spectroscopic ellipsometry from which a bandgap of 705 nm (1.76 eV) has been measured[57]. The slight shift in the bandgap value compared to pure $CsPbI_3$ (1.71–1.73 eV) is attributed to the incorporation of the EuI_2 additive, which reduces the crystallite size from 89 nm to 58 nm[9,56,58]. Small perovskite crystallites are expected with a wider bandgap compared to large ones due to quantum confinement and size-dependent structural effects, as reported in ref. 59. It is worth noting that the average

https://doi.org/10.1038/s41467-025-56227-9

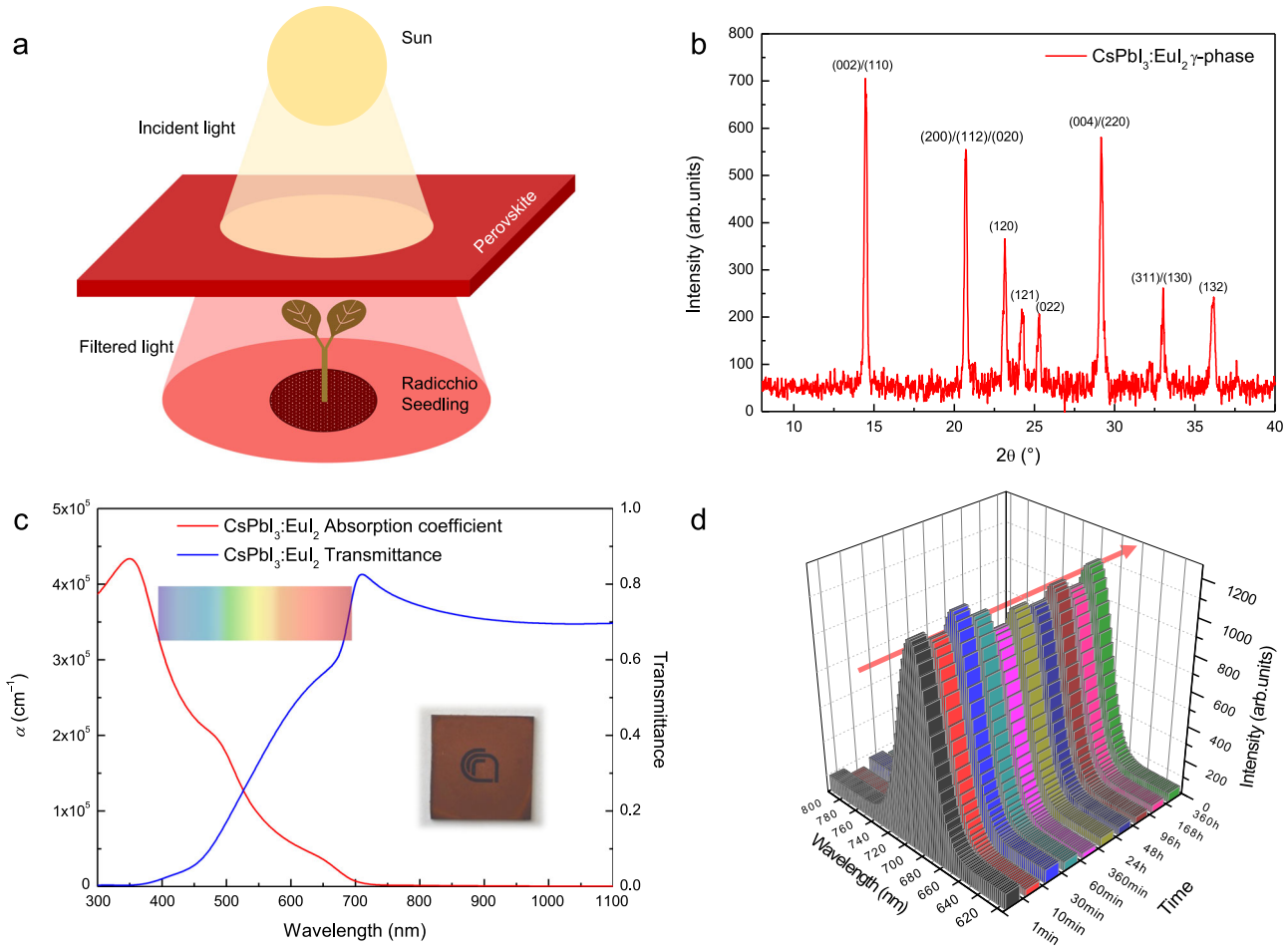

Fig. 1 | Comprehensive analysis of $CsPbI_3$:EuI_2 perovskite layer: experimental scheme, structural, optical, and photoluminescence properties. a Conceptual scheme of the experiment. **b** XRD pattern of $CsPbI_3$:EuI_2 perovskite layer. **c** Absorption coefficient (red) and transmittance (blue) spectra of the $CsPbI_3$:EuI_2 perovskite layer (see photograph in the inset) within the range 300–1100 nm. **d** Representative photoluminescence measurements of $CsPbI_3$:EuI_2 perovskite layer over 360 h (15 days). Source data are provided as a Source Data file.

transmittance of the layer is still 70–80% in the region below the bandgap (far-red/infrared) while it is 32% in the visible range (AVT), which allows light to pass through for the benefit of the seedlings placed underneath. The absorption and transmittance profile would thus enable the $CsPbI_3$:EuI_2 to achieve high efficiency, together with a further prospected benefit for the growth of the seedlings[60]. We then investigated the stability of the perovskite layer in N_2 environment at room temperature by monitoring the characteristic photoluminescence (PL) peak of $CsPbI_3$:EuI_2 at 699 nm over the timeline of the experiment (15 days). Figure 1d shows that the average PL intensity remains constant, thus assuring stable filtering conditions towards the seedlings[58,61–63]. In addition, Supplementary Fig. 2 compares scanning electron microscopy images and X-ray diffraction patterns (extracted lattice parameters in Supplementary Table 1) at t_0 and after 15 days, further highlighting the stability of the perovskite layer over the experiment period. Finally, to prove the thermal stability of the $CsPbI_3$:EuI_2 layers, we performed accelerated thermal stress tests. The optical behavior was also monitored over time via in-situ isothermal spectroscopic ellipsometry measurements, tracking the evolution of α in a dry N_2 atmosphere. Supplementary Fig. 3 shows α with negligible changes after 225 min at 90 °C or 150 min at 100 °C.

Growth of radicchio under perovskite greenhouse rooftop

The 130-nm thick $CsPbI_3$:EuI_2 perovskite layers were thus applied on the rooftop of the laboratory-scale greenhouse. This rooftop consists of four perovskite-covered glass panels arranged side by side, 2.5 × 2.5 cm^2 each. In a twin system to be used as a reference, a pure glass rooftop made of four bare glass panels is applied. Glass substrates were used as reference since they represent the support of the perovskite films. Furthermore, bare glass covers closely simulate the greenhouse rooftop. On the other hand, leaving the seedling in an open field would change the local ambient conditions and risk altering the comparison. The experiment aims to evaluate the growth of radicchio seedlings, starting from germinated seeds, within the laboratory-scale greenhouse under the perovskite rooftop (P sample), in comparison with the growth of similar seedlings under the bare glass rooftop (G sample). Both groups undergo light/dark cycles with 16/8 h for 15 days to mimic real-life sunlight conditions, and 3 replicates were repeated for each Magenta™ box (Fig. 2a, b).

To preserve the photoactive phase, the $CsPbI_3$:EuI_2 rooftop is locally kept under a dynamic N_2 flow to prevent any degradation due to humidity exposure[58]. The entire experiment is performed indoors at a constant ambient temperature of 24 °C and 40% RH. Radicchio seeds were preliminarily subjected to a pre-germination process for three days under dark conditions. Following this period, the best-germinated seeds were gently buried in organic soil made of 70% peat and 30% sterile sand, which was placed inside Magenta boxes with internal white walls simulating the greenhouse environment with multiple light reflections. Air circulation was assured through small lateral hollows. The organic soil was seeded at a density of 2 seeds/cm^2 to a depth of 1 cm, resulting in a total of 4 seeds sown within each box. We replicated the experiment 5 times. We used 10 Magenta boxes (5 G-

https://doi.org/10.1038/s41467-025-56227-9

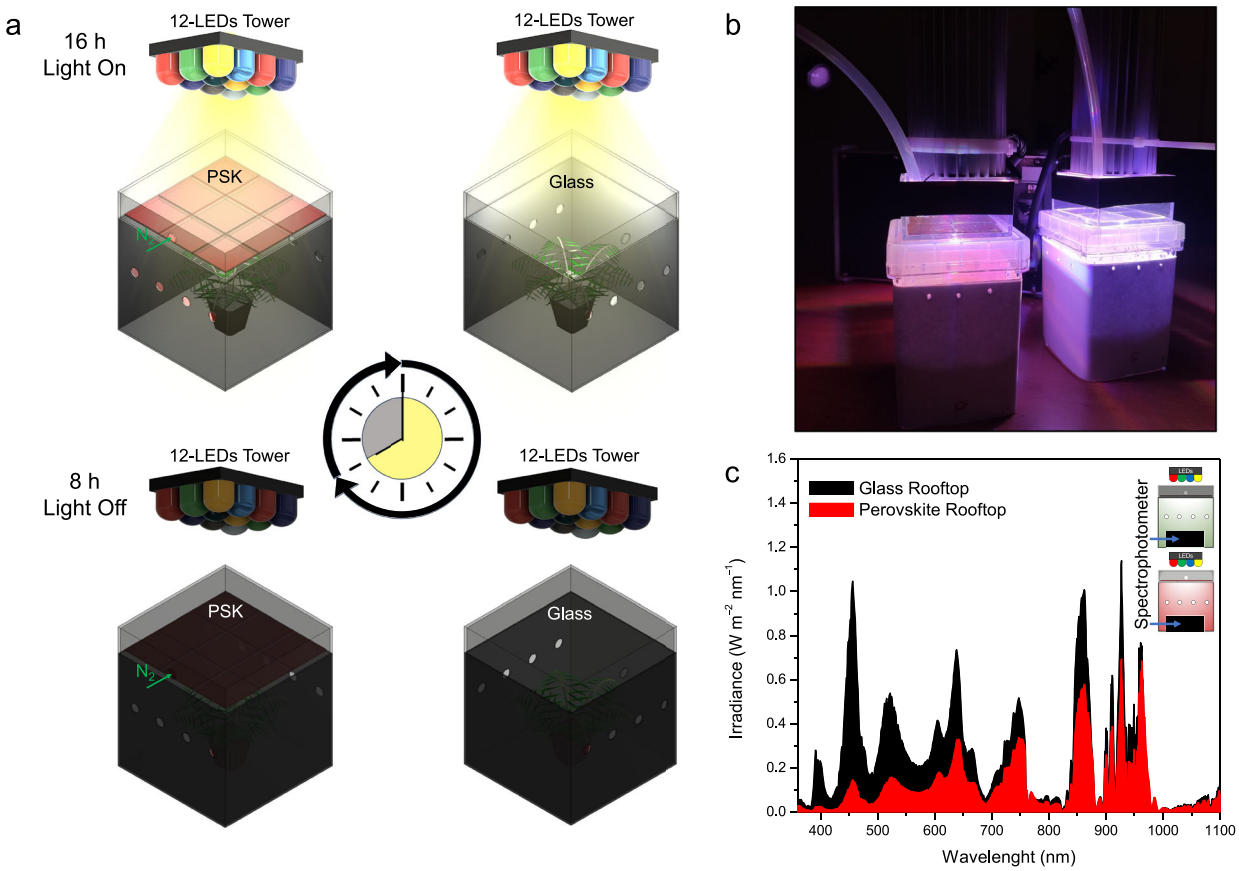

Fig. 2 | Experimental setup for radicchio cultivation under perovskite greenhouse rooftop: schematic, photos, and light transmission spectra. Schematic view (**a**) and photos (**b**) of the experimental setup consisting of a laboratory-scale greenhouse with the ST-PSC-coated and glass bare rooftop where radicchio seedlings are cultivated under illumination (16h/8h light/dark cycle) from a 12-LEDs source. **c** Irradiance spectra of 12-LEDs source light passing through the glass (black) and perovskite (red) greenhouse rooftop. Source data are provided as a Source Data file.

sample, 5 P-sample) each containing 4 seedlings. This seeding density was chosen to ensure adequate spacing for subsequent growth while maximizing the box space. Throughout the 15 days, a total volume of 100 ml of water was provided to the seedlings. Detailed chemical and physical properties of the water utilized are provided in Supplementary Table 2. The germinated seeds are thus separately illuminated over the perovskite and reference glass-covered boxes, by 12-LEDs tower, which acts as solar simulator. The white walls of the box facilitate the mixing and uniform distribution of the light components. For the G sample, the LED tower directly illuminates the seedlings under the glass rooftop, while for the P samples the light is partially filtered by the photoactive perovskite layer before reaching the seedlings. This difference is evident through the varied color of the filtered light: reddish for the perovskite rooftop and white for the glass rooftop (Fig. 2b). The overall LEDs power is preliminary calibrated through a spectrometer placed under the glass rooftop to replicate the Air Mass (AM) 1.5G spectral output of the sun according to the International Standard IEC 60904-9 Class A (Supplementary Fig. 4 for detailed calibration values). The total irradiance of the LED tower is adjusted to mimic real-world solar conditions at the soil level following NREL data specific for Treviso (Italy), a city renowned for radicchio cultivation[64,65]. Specifically, the day/night cycle is simulated by providing 16 hours of irradiation at 190 Wm^{-2}, followed by 8 hours of darkness[66,67], resulting in a cumulative daily irradiance of 3040 Whm^{-2}, which effectively mirrors the average natural light conditions in Treviso (mean annual solar radiation at a tilt angle of 0° being 3000 $Whm^{-2}day^{-1}$)[65]. Figure 2c depicts irradiance spectra of light passing through the glass and perovskite layer, which thus reaches the radicchio seedlings in the two cases. In the wavelength range below the bandgap 700–1100 nm, the perovskite rooftop largely allows incident light to pass through due to its low absorption capability (far-red to infrared). In particular, the integrated irradiance value in the range 700–1100 nm is 59 Wm^{-2} under the perovskite compared to 87.4 Wm^{-2} under the glass, with the perovskite layer enabling 67.5% irradiance passing through it. On the contrary, as expected, the perovskite rooftop shows a reduction of the irradiance in the PAR range (400–700 nm) with an integrated irradiance value of 31.5 Wm^{-2} under the perovskite and 96.7 Wm^{-2} under the glass (32.6% of transmitted light). In the UV range between 360 and 400 nm, perovskite exhibits high absorption, allowing only 15.8% of the incident light to pass through, in contrast to the glass rooftop (0.6 Wm^{-2} vs. 3.8 Wm^{-2}). Partial absorption by perovskite layer thus alters the overall spectral composition of the transmitted light (Fig. 2c) and, accordingly, the total irradiance decreases to a value of 92 Wm^{-2} [68], with a reduction of 52% with respect to the reference glass rooftop (190 Wm^{-2}). This irradiance decrease frames the $CsPbI_3$:EuI_2 layer[69] behavior in interacting with the solar light. Both spectra exhibit identical irradiance intensities at the beginning and the end of the experiment (after 15 days) (Supplementary Fig. 5.). The internal greenhouse temperature under irradiation is stable at 26 °C in both kinds of setups. This illumination protocol ensures that the seedlings are exposed to light conditions that mimic real-world scenarios.

Figure 3a depicts the growth evolution of radicchio seedlings under perovskite and glass rooftops at t_0 (i.e., at the beginning of measurements) in the form of germinated seeds and after 7 (Fig. 3b) and 15 (Fig. 3c) days under 16h/8h light/dark cycles. After 7 days, all germinated seeds under both glass and perovskite rooftop have grown to seedlings with two small leaves each. At day 15, all radicchio seedlings under the glass rooftop display two leaves per stem, whereas

https://doi.org/10.1038/s41467-025-56227-9

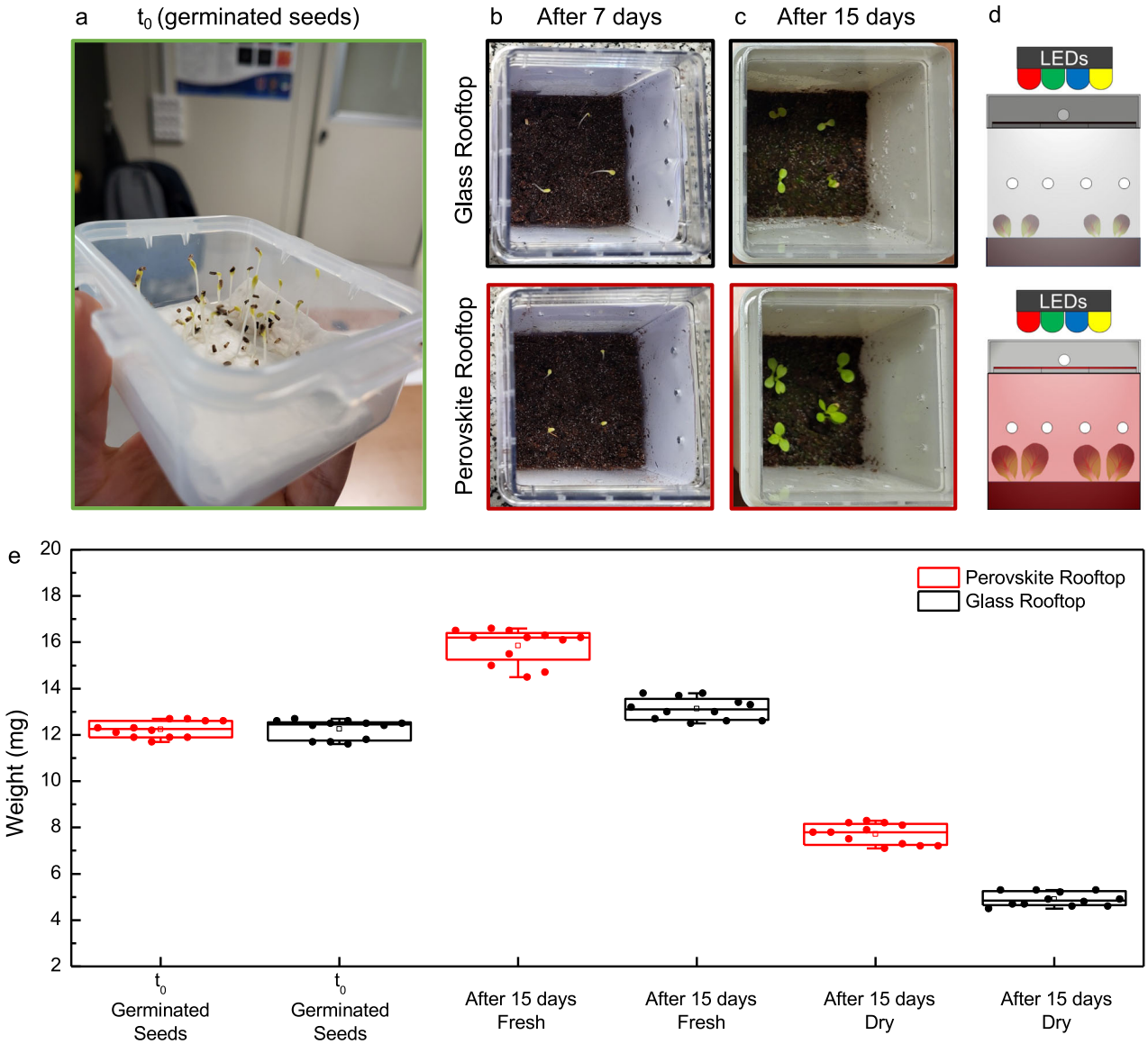

Fig. 3 | Growth and weight progression of radicchio seedlings under perovskite and glass rooftops over 15 days. a Photo of radicchio seedlings at t_0 (germinated seeds). **b** After 7 days of 16h/8h light/dark cycles under perovskite and glass rooftops. **c** After 15 days of 16h/8h light/dark cycles under perovskite and glass rooftops. **d** Schematics of experimental setups. **e** Weight of the seedlings grown under glass (black) and perovskite (red) rooftop at time t_0 (seeds germinated) and after 15 days freshly measured and after drying. We utilized 12 seedlings samples for each experiment phase, resulting in a total of $n = 72$ seedlings. Data are presented as box plots (center line at the median, upper bound at 75th percentile, lower bound at 25th percentile) with whiskers at minimum and maximum values. Mean value is represented as a square. Source data are provided as a Source Data file.

those under the perovskite rooftop show flourishing growth with 3–4 larger leaves. The measured average increase for each leaf area is 25% (Supplementary Fig. 6) per stem. The stem lengths are comparable between the two samples (2 ± 0.2 cm). All three replicates of the experiment consistently provided similar results, thus further corroborating our findings. Figure 3d shows a schematic of the experiment. The biomass of the seedlings was measured and Fig. 3e shows greater biomass production both fresh and dry for the seedlings grown under perovskite (Supplementary Movie 1) in all replicates. In the literature[70,71], it was reported that plant productivity generally increases with higher daily light integral of PAR. This is not our case, because the daily light integral received by radicchio seedlings under the perovskite rooftop is even notably lower than that under the glass rooftop (Fig. 2b). This finding shifts the focus to the influence of the light spectral composition on plant morphology and adaptive responses, better known as photomorphogenesis[72]. The main differences between the light filtered by the perovskite rooftop compared to the glass rooftop are 1) the small amount of UV component and 2) the different spectrum in the PAR range. For the first, it was reported in the literature that plant UV-B responses generally aim at protecting sensitive tissues from UV-B penetration and repairing UV-B induced damage. UV-B protection is mainly achieved by epidermal accumulation of UV-absorbing flavonoids and hydroxycinnamic acids[73]. In particular, UV-B radiation can also reduce plant height and leaf area in different plant species due to its influence on growth regulators and signaling pathways[74]. On the other hand, the study by Laurenvcikova et al.[31] demonstrated that UV radiation, particularly UV-B, might influence the accumulation of secondary metabolites in lettuce and radicchio plants. We investigated the UV influence on early-stage radicchio seedling growth with a focused experiment, in which the UV LEDs are turned off compared with the reference case with the UV LEDs left on. The results show no difference between the two conditions in terms of leaf surface area and seedling weight, indicating that the absorption of the UV by perovskite rooftop has a minimal effect on the

observed increased leaf surface area and on the higher number of leaves (Supplementary Fig. 7). This finding moves the focus to the PAR range of light. Blue and red/far-red light, in particular, affect plant development, influencing properties such as leaf area, stem length, and flowering according to Ref. 49. Mixtures of red (R) and blue (B) light generally result in higher biomass and photosynthetic rates compared to monochromatic light[64,75]. In particular, a spectrum deficient in blue light and abundant in red light may stimulate the growth of larger leaves by promoting cellular expansion[66]. The optimal R/B ratio is different among species: for example, it has been reported in literature that in lettuce the shoot dry weight increases with increasing R/B ratio, reaching a maximum at R/B= 12, with the increase primarily ascribed to larger leaf area and a greater number of leaves[76]. In addition, the red/far-red ratio is reported to regulate plant development through shade-avoidance responses, impacting extension growth[77]. On this basis, we disclose that the enhanced growth of radicchio seedling leaves benefits from the filtering action by the $CsPbI_3$:EuI_2 perovskite rooftop in the PAR range compared to the full light passing through the glass rooftop, with the promotion of favorable photomorphogenic responses. Despite the lower daily light integral, we thus conclude that the deficiency in blue light, the relative abundance in red light, and the lower red/far-red intensity ratio in the filtered spectrum (Fig. 2c) positively contribute to the observed flourishing growth in the greenhouse environment. These findings entail that integrating Cs-based perovskite rooftops can increase radicchio plant productivity, through enhanced photosynthesis and biomass production, which are essential for crop yield and overall agricultural output.

RNA-sequencing of the seedlings grown under perovskite rooftop

To investigate the transcriptomic differences between the radicchio plant's growth under glass and perovskite rooftop, we performed RNA-sequencing on the two kinds of samples. Sequencing of radicchio RNA samples produced an average of 31,057,247 reads per sample (ranging from 23,321,414 to 36,829,272) (Supplementary Data 1). Reads aligned to the reference genome resulted in an average mapping rate of 71.20% (ranging from 65% to 81% Supplementary Data 1). Normalized read counts are reported in Supplementary Data 2. Multidimensional analysis (Principal component analysis, PCA) on read count data showed no distinct clusters and a large variability across all samples (Supplementary Fig. 8), as also highlighted by the heatmap depicting the transcript abundance in the different samples, which showed a similar transcriptomic response of both samples, grown under glass and perovskites (Fig. 4).

Using G samples as a reference and a cut-off of the *p*-adjusted value ≤ 0.05 to classify a gene as differentially expressed (DEG) in comparison with the control, 22 genes were found to be differentially regulated. Among them, 9 were identified as up-regulated and 11 as down-regulated in P samples compared to G samples (Supplementary Data 3).

Among the 9 up-regulated DEGs, a RAS-related protein[78] RAB-B1c related gene (Log2FC= 5.30) was found to be the most up-regulated in P samples. In *ARABIDOPSIS*, a model organism for understanding gene expression in plants, the gene *RAB-B1c*[79] is known to be influenced by light conditions, having been reported to be downregulated in the dark when compared to light conditions[80]. Other up-regulated genes include a gene putatively coding for a tropinone reductase homolog *At5g06060-like* (Log2FC = 4.23), involved in alkaloid metabolism, a gene coding for a senescence-specific cysteine protease *SAG39-like* (Log2FC= 3.58), a gene coding for a NAC domain-containing protein (Log2FC = 1.65), and a gene coding for a universal stress protein A-like protein (Log2FC=1.05), all putatively involved in different metabolic pathways, including plant response to environmental stress. It is worth noting that *SAG39* has been reported to negatively regulate leaf senescence, delaying this process, mainly by regulating the stability of Chl-protein complexes[81]. The up-regulation of the gene coding for a BRI1 kinase inhibitor 1-like (Log2FC = 1.43) suggested a regulatory constraint on the brassinosteroid pathway, which is essential to plant growth. In plants, BRI1 is a protein localized to the plasma membrane and its kinase activity has an essential role in brassinosteroids-regulated plant growth and development[82]. On the other hand, BRI1 kinase inhibitor 1 (BKI1), a membrane-associated protein, is known to be a negative regulator of BRI1[83]. In addition, a gene coding for a plastocyanin B'/B" (Log2FC =1.24) showed up-regulation, suggesting a remodeling of the photosynthetic electron transport chain. Lastly, a gene coding for an aquaporin *PIP2-1-like* was found to be up-regulated in P samples (Log2FC = 1.11), suggesting an improved transport of water across cell membrane[84].

On the other hand, among the 11 down-regulated genes, a gene encoding an early light-induced protein 2, (Log2FC = −2.11), was identified. The regulation of this gene is generally associated with the early stages of light response[85]. It has been reported that the accumulation of Early Light-Induced Protein 2 (Elip2) is triggered when PSII reaction centers are photodamaged, suggesting that Elip2 plays a role in the plant defense response to light-induced stress[86]. A down-regulation of this gene may suggest that the plants have adapted to the perovskite-filtered light conditions. Other genes identified as down-regulated were genes coding for a NAC domain-containing protein 17-like (Log2FC: −2.92), an AT-hook motif nuclear-localized protein (Log2FC: −3.06), a berberine bridge enzyme-like (Log2FC: −3.20), a scopoletin glucosyltransferase-like (Log2FC: −3.50), an asparagine synthetase (Log2FC: −3.52), a protein PHOSPHATE-INDUCED (Log2FC: −3.66) a cysteine-rich receptor-like protein kinase 2 (Log2FC: −4.60), a callose synthase (Log2FC: −4.64). Down-regulation of these genes might imply a reduction in these processes, suggesting a role in the adaptation to the growth condition under perovskite. A down-regulation was also observed for a gene encoding an alpha-copaene synthase (Log2FC: −8.78), a key enzyme in the synthesis of terpenoids[87], which might suggest that the synthesis of these compounds is affected by the perovskite-filtered light.

Overall, the gene expression differences observed in radicchio seedlings grown under glass and perovskite rooftops indicate adaptive responses of the plants to environmental variations, particularly in response to light conditions and stress factors associated with rooftops.

Photovoltaic production of perovskite greenhouse rooftop

As a first step to evaluate the photovoltaic production of the perovskite rooftop, the 130-nm thick $CsPbI_3$:EuI_2 perovskite layer is integrated into a simulated ST-PSC architecture. While the simulations are meant to model a best-case scenario of device, where effects of charge trapping or ionic migration are negligible, the integrated properties of the materials are taken from a realistic case of PSC architecture (e.g. Fig. 1). The structure of the simulated device is depicted in Fig. 5a. It consists of a planar n-i-p architecture on a glass substrate in which the perovskite layer is sandwiched between a 50 nm-thick titanium dioxide (TiO_2) film acting as electron transporting layer and a 25-nm-thick Poly[bis(4-phenyl)(2,4,6-trimethylphenyl)amine (PTAA) film acting as hole transporting layer. A 300 nm F-doped tin oxide (FTO) and a 100 nm Indium tin oxide (ITO)[88] are chosen as the transparent bottom and top electrodes, respectively. A glass layer is added on the ITO top electrode to consider the cover glass required for PSC encapsulation[89]. The thickness of the transporting layers and electrodes was set based on values reported in the literature for similar ST-PSCs[90]. The perovskite optical properties (real and imaginary parts of the refractive index, i.e., n and k) used in the simulations were determined by spectroscopic ellipsometry while those of the other layers are extracted from the literature (Supplementary Fig. 9 and Supplementary Table 3). Figure 5b shows the comparison of the absorbance and transmittance spectrum for the full FTO/TiO_2/$CsPbI_3$:EuI_2/PTAA/ITO

https://doi.org/10.1038/s41467-025-56227-9

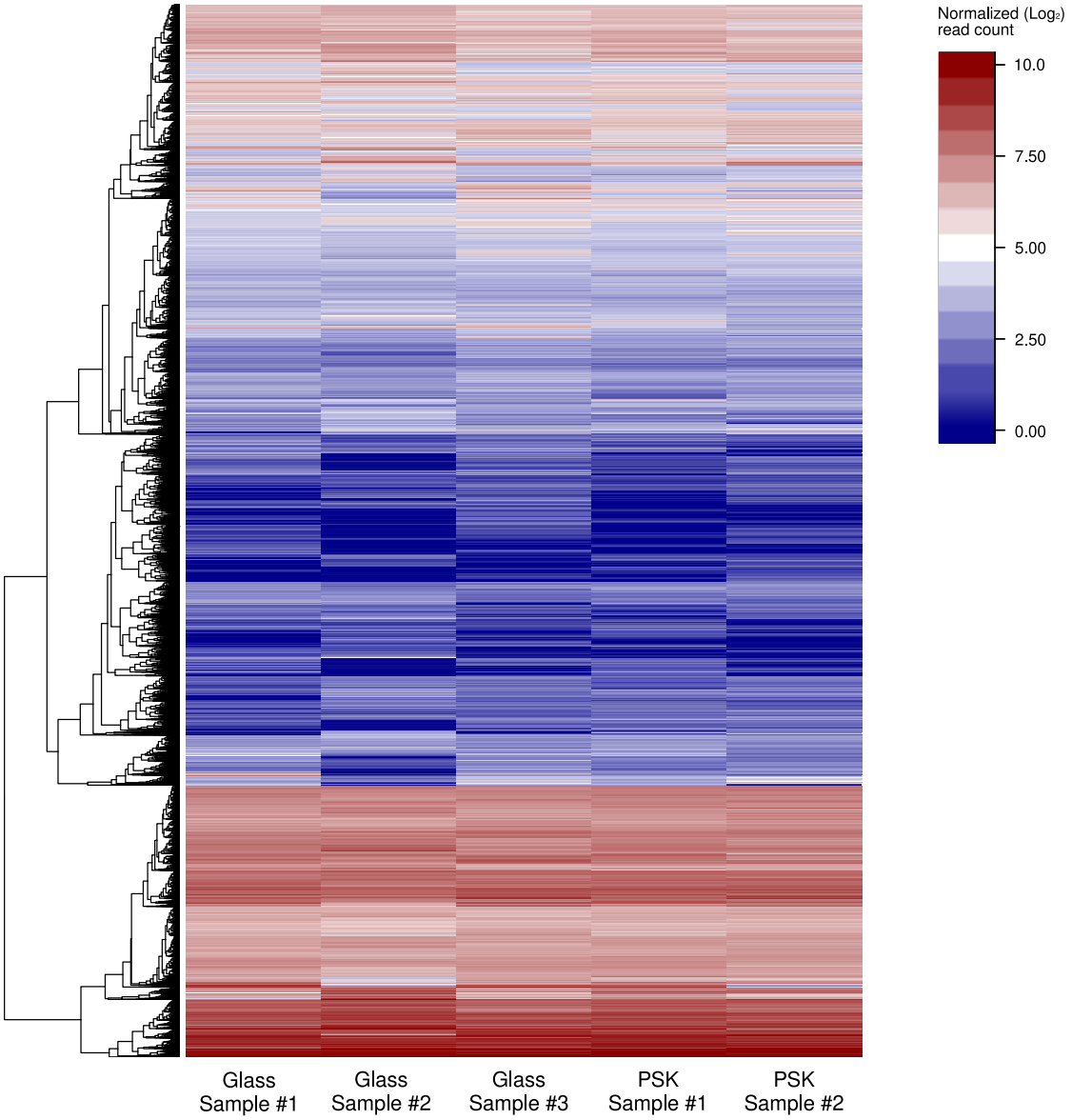

Fig. 4 | Heatmap of transcript abundance and hierarchical clustering in RNA samples. Heatmap depicting read count (Log2 transformed) in the five RNA samples. Hierarchical clustering of transcripts was performed using the McQuitty algorithm. The heatmap shows the transcript abundance across the five samples, with red levels indicating a high number of reads assigned to the specific genes and blue representing a low number. Source data are provided as a Source Data file. In the x-axis label PSK=perovskite.

device and only the $CsPbI_3$:EuI_2 layer. The full device shows enhanced absorption in the range 350–450 nm due to PTAA absorption and in the range 710–1100 nm due to FTO and ITO absorption, as shown in Supplementary Fig. 10. It is worth highlighting that the transmittance of the entire device is almost identical to that of the isolated perovskite layer within the 300–900 nm range, and this enables us to extend the findings on the seedlings' growth also to the complete device architecture. This comes from the specific threshold of each material absorption, being the bandgap of the transporting layers and the electrodes in the UV range (< 400 nm), whereas the perovskite layer is the main one interacting with the incident light in the visible range. The current density-voltage (J-V) curve simulated under 1 sun and AM 1.5G spectrum conditions for the $CsPbI_3$:EuI_2 ST-PSC is presented in Fig. 5c, along with the photovoltaic parameters. The device exhibits an open-circuit voltage (V_{OC}) of 1.16 V, a short-circuit current (J_{SC}) of 14.03 $mAcm^{-2}$, and a Fill Factor (FF) of 77.93%, yielding a power conversion efficiency of 12.67%. This efficiency value aligns well with that of ST-PSCs reported in the literature fabricated using similar perovskite thicknesses but varying perovskite compositions or device architectures[90,91] (Supplementary Note 1, Supplementary Fig. 11 and Supplementary Table 4).

After characterizing the $CsPbI_3$:EuI_2 ST-PSC, we simulated its real-world application as a perovskite PV greenhouse rooftop located in Treviso (Italy), monitoring the photovoltaic performance for one year. A rendering of the photovoltaic greenhouse with its main source of energy consumption (heating/cooling, illumination, irrigation) is represented in Fig. 6a. Figure 6b illustrates the monthly solar radiation integrated over 280–1150 nm wavelength range incident on the $CsPbI_3$:EuI_2 perovskite PV rooftop and transmitted through it. Figure 6c provides an in-depth analysis, displaying the transmitted solar irradiance spectrum under the $CsPbI_3$:EuI_2 perovskite PV rooftop over a year with a 2-hour resolution, while Fig. 6d depicts the wavelength-

https://doi.org/10.1038/s41467-025-56227-9

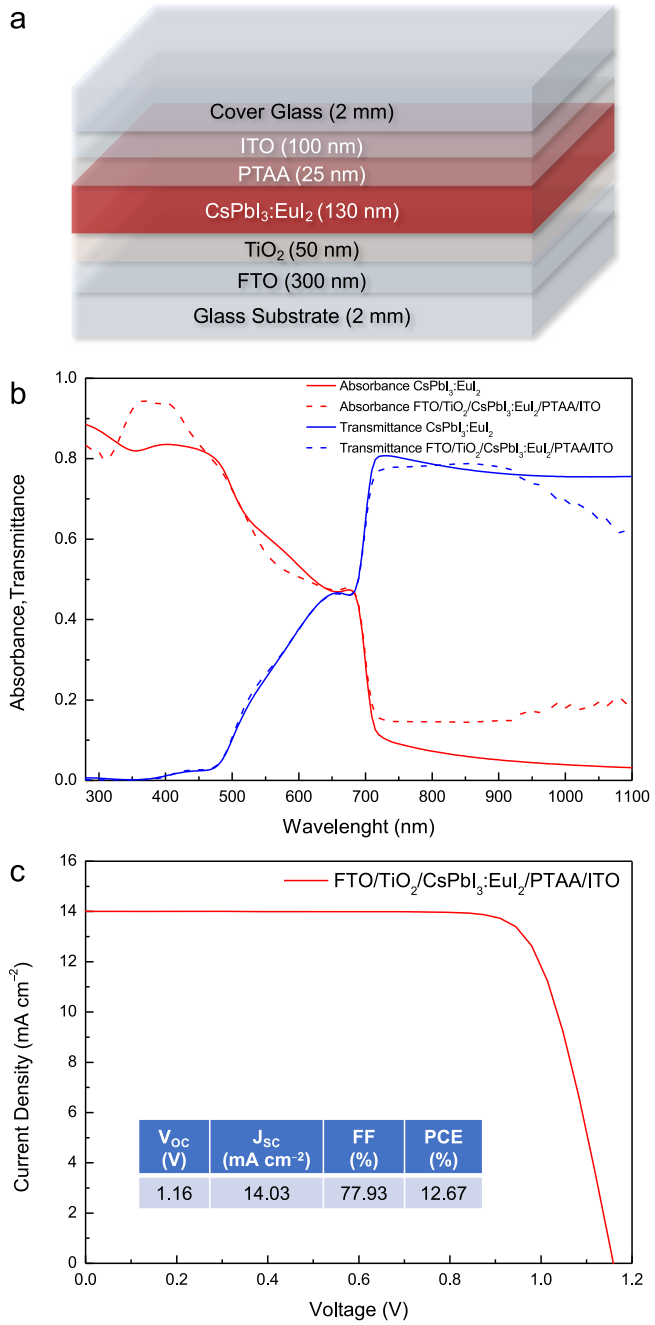

Fig. 5 | Simulation and performance analysis of the ITO-PTAA-$CsPbI_3$:EuI_2-TiO_2-FTO device. a Schematics of the simulated ITO-PTAA-$CsPbI_3$:EuI_2-TiO_2-FTO device structure. **b** Transmittance (blue) and absorbance (red) spectra perovskite and device. **c** *JV* characteristic of the device. Photovoltaic parameters are also indicated.

resolved solar radiation obtained by integrating this spectrum over the same period. On the one hand, the spectral and integrated data of the light transmitted through the $CsPbI_3$:EuI_2 perovskite PV rooftop are crucial, as they represent the solar radiation that illuminates the radicchio plants, thereby influencing their growth and development. On the other hand, the absorbed light is directly related to the generation of electric energy by the $CsPbI_3$:EuI_2 perovskite PV rooftop. Photovoltaic energy generation for each month is depicted in Fig. 6e, with related values listed in Table 1.

The lowest photovoltaic output of the $CsPbI_3$:EuI_2 perovskite PV rooftop is recorded in December (5.9 $kWhm^{-2}$), while the highest is observed in June (34 $kWhm^{-2}$), with intermediate values throughout the year. The photoconversion efficiency (calculated as the ratio between the monthly integrated generated electric power and incident solar radiation) varies over the year as shown in Table 1. The average value of 12.75%, as expected, is very close to the value of 12.67% obtained for 1 sun illumination (see Fig. 5c). The estimated total annual energy production of the $CsPbI_3$:EuI_2 perovskite PV rooftop amounts to 220–243 $kWhm^{-2}$, which takes into account the possible inaccuracies in the simulated performance (Supplementary Note 1). Typically, greenhouse cultivation involves substantial energy usage for tasks such as heating, cooling, irrigation, and lighting[92]. According to literature[93], annual energy consumption in European Union (EU) greenhouses for cultivating leafy greens like radicchio or lettuce ranges from 1 $kWhm^{-2}$ to 5 $kWhm^{-2}$ for low-energy intensity structures and from 83 $kWhm^{-2}$ to 222 $kWhm^{-2}$ for high-energy intensity greenhouses, with variations based on geographical location. Thus, the projected total annual production of the $CsPbI_3$:EuI_2 perovskite PV rooftop (243 $kWhm^{-2}$) would fulfill the energy needs of high-energy intensity greenhouses, exceeding by nearly two orders of magnitude those of low-energy intensity. In 15 days, the duration of our experiment, the greenhouse rooftop would produce 16 $kWhm^{-2}$. In indoor applications at different illuminance conditions (white LED of 1000-500-200 lux), the PCE of $CsPbI_3$:EuI_2 ST-PSC would be 21–22%. The generated electricity through indoor greenhouse illumination could thus power sensors for overnight ambient monitoring (Supplementary Fig. 12).

Discussion

We have thoroughly examined the application of semitransparent $CsPbI_3$:EuI_2 perovskite layers as photoactive materials for Agrivoltaics, and we have provided their proof-of-concept application on the growth of radicchio seedlings into laboratory-scale greenhouses. We transversely focused on the structural/optical, agricultural, and photovoltaic aspects of this application. Through advanced structural and optical characterization, we have shown the high crystalline quality of the perovskite material and the positive tradeoff between absorption (bandgap at 705 nm) and transmittance achieved by using a Cs-based perovskite formulation, within the photosynthetically active radiation range for crop growth. The observation of radicchio seedling growth, from pre-germinated seeds under simulated sunlight, indicates enhanced development of leaves area and an increase in weight under the perovskite rooftop compared to the reference (bare glass rooftop). This result demonstrates the beneficial influence of the light spectrum filtered by the perovskite layer on seedling's photomorphogenesis, to be mainly ascribed to the recorded deficiency in blue light, the abundance in red light, and the lower red/far-red intensity ratio. Although the overall transcriptomic profile is almost similar between the two tested conditions, specific responses are suggested by the expression patterns of 9 genes detected as *DEGs* comparing P samples vs the G ones. These genes likely associated to different environmental stress responses, metabolic pathways, growth regulation, and light perception exhibited different regulation patterns under perovskite conditions, indicating a physiological adjustment in the seedlings. Beyond the demonstrated impact in the first stage of the plant life cycle, results are promising and pave the way for further multidisciplinary studies dedicated to the use of perovskite for crop production in indoor environments. In the multidisciplinary approach, through real-world simulations of $CsPbI_3$:EuI_2 integrated into ST-PSC, we additionally estimated a projected annual clean energy production from perovskite PV greenhouse rooftop of 243 $kWhm^{-2}$ pairing the requirements of high-energy intensity greenhouses (83–222 $kWhm^{-2}$) for heating/cooling, illumination and irrigation needs. In summary, our study frames the advantages of integrating semitransparent $CsPbI_3$:EuI_2 perovskite into greenhouse rooftops for enhancing seedling growth and physiological responses, and for simultaneous self-production of clean energy at the cost of affordable technology. This study sets the stage for an extension to large-scale systems under real conditions.

https://doi.org/10.1038/s41467-025-56227-9

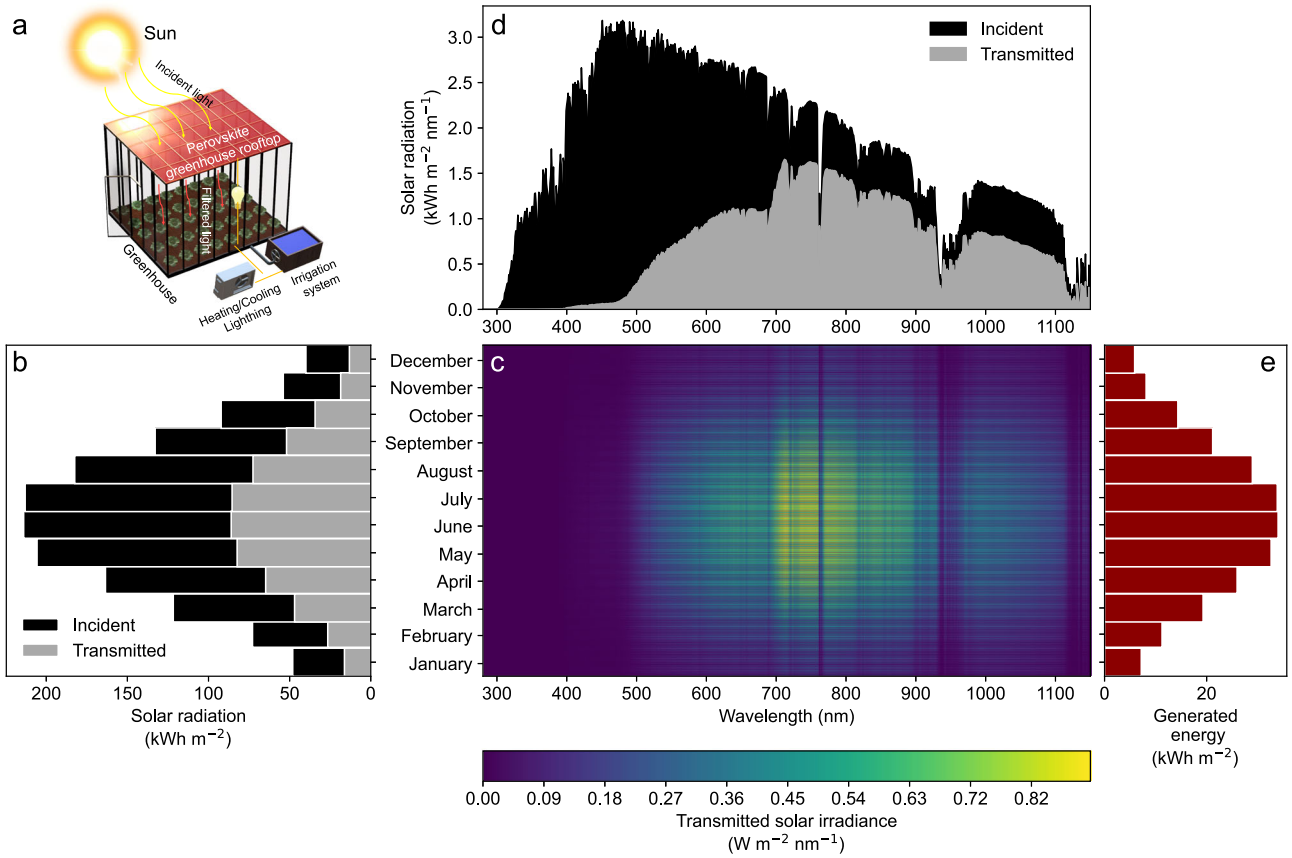

Fig. 6 | Perovskite PV Greenhouse: solar radiation dynamics and energy generation over a year. a Rendering of the real-world application of perovskite PV rooftop on a greenhouse for the maturation of plants. **b** Incident (black) and transmitted (gray) monthly solar radiation. **c** Transmitted solar irradiance spectrum as a function of time, over one year, with 2h resolution. **d** Wavelength-resolved solar radiation is obtained by integrating transmitted solar irradiance spectrum over one year. **e** Monthly photogenerated electric energy.

Methods

Fabrication of perovskite films

A solution containing 1 M PbI_2 (Tokyo Chemical Industry) and 1 M CsI (Tokyo Chemical Industry) was prepared by blending them in a composite solvent made of DMF and DMSO (3:1 v/v). Additionally, a solution of 0.1 M EuI_2 (Sigma-Aldrich) was prepared using the same mixed solvent of DMF and DMSO (3:1 v/v). These solutions were stirred at room temperature for 1 hour. Then, 1 ml of the PbI_2/CsI solution was combined with 0.5 ml of the EuI_2 solution to achieve the desired stoichiometry, followed by stirring for another 1 hour[94]. The entire preparative was performed in ambient air (35% RH). The deposition of the perovskite film was carried out by spin-coating the precursor solution onto bare glass substrates (Corning 2947, transmittance > 90%) in two stages: initially at 1000 rpm for 10 seconds, followed by 5000 rpm for 25 seconds in an N_2-filled glove-box[95]. The film was subjected to two-step annealing (90 °C for 15 min and 350 °C for 1 min) and rapidly cooled to room temperature to form the photo-active phase of $CsPbI_3$:EuI_2.

Table 1 | Photovoltaic energy generation for each month

Month	Incident solar radiation (kWh/m²)	Generated PV energy (kWh/m²)	Photoconversion efficiency (%)
January	59.0	7.1	12.17
February	89.1	11.2	12.62
March	148.6	19.3	12.99
April	199.5	25.9	13.02
May	250.8	32.6	13.01
June	260.8	34.0	13.04
July	259.7	33.8	13.03
August	222.5	28.9	13.01
September	162.1	21.1	13.06
October	112.7	14.3	12.74
November	66.1	8.1	12.30
December	49.1	5.9	12.00
TOT:	1880.4	242.7	–

X-ray diffraction

X-ray diffraction (XRD) patterns were acquired using a SmartLab (Rigaku) diffractometer equipped with a 9 kW rotating anode Cu X-ray source operating at 45 kV and 100 mA, along with a HyPix-3000 detector. The recording step size for the patterns was configured at 0.01°, with an acquisition speed of 0. 1° per minute[96].

Photoluminescence spectroscopy

Photoluminescence Spectroscopy measurements were performed using a commercially available instrument (Arkeo, Cicci Research s.r.l.). The samples were excited with a green laser (532 nm) at an incident angle of 45 degrees, generating a circular spot with a diameter of 1 mm. After a waiting period of 1000 ms, the PL signal was recorded using a spectrometer.

Spectroscopic ellipsometry

We used a V-VASE, J A Woollam spectroscopic ellipsometer equipped with an autoretarder for optical characterization. To prevent degradation from exposure to humid air, the sample was enclosed in a sealed chamber with an overpressure of N_2. Optical constants were assessed across the 190–2500 nm spectral range to construct a comprehensive model. Considering that the sample was deposited on glass, appropriate adjustments were made to account for potential light interaction with the back surface of the glass slide. The thickness of the perovskite was determined by ensuring adherence to the Cauchy equation for the refractive index in the transparent region, maintaining consistency for subsequent evaluation of an optical model consistent with Kramers-Kronig relations[97–99], based on a multiple critical point parabolic band. We calculate the absorption coefficient from the ellipsometer dielectric function (ϵ_1 and ϵ_2)[100,101]. The average visible transmittance was calculated from the simple arithmetic mean of the transmittance in the 400-800 nm range[91].

Laboratory scale greenhouse and Illumination setup

Magenta™ GA-7 boxes are used to build up laboratory-scale greenhouses. The internal walls are white-painted to enable multiple light reflections as in real greenhouses. Air circulation is assured through small hollows, a few millimeters in diameter. An organic soil made of 70% peat and 30% sterile sand is placed at the basis of the boxes and is seeded at a density of 2 seeds/cm^2, resulting in a total of 4 seeds sown within each box. A glass rooftop, with or without perovskite coverage, is located in the uppermost part of the greenhouse, connected to a pipeline of pure nitrogen that assures a dynamic flux of gas to preserve the perovskite layer from degradation. In an outdoor case, encapsulated perovskite would be used. Immediately over the rooftop, simulated sunlight for plant illumination is provided by a LEDs tower placed over the rooftop (Cicci Research srl) made of 12 LEDs, specifically made of Warm White (> 4750K), Cool White (< 3750K), Far UV (360-370nm), UV (380-390nm), Deep Blue (445-465nm), Green (490-535nm), Amber (580- 600nm), Red (620-630nm), Hyper Red (650-670nm), Far-Red (720-740nm), IR (840-870nm), Far IR (925-955nm).

Spectrophotometer

A spectrophotometer, provided by Cicci Research s.r.l., was used to acquire the light spectrum reaching the plants in the G (under glass) and P (under perovskite) samples. The spectrometer is placed at the same height of radicchio seedlings to measure the spectral irradiance of the light coming from 12 LEDs Tower. The measurements were carried out in a spectral range from 330 nm to 1100 nm with a spectral resolution of 1 nm and an integration time of 10 ms.

Photovoltaic production simulation

Photovoltaic devices were simulated using the 1D electro-optical simulator Setfos (v5.4.12) by Fluxim[102], which self-consistently combines the drift-diffusion formalism for charge transport with the transfer-matrix formalism for optical absorption/transmission. The wavelength-dependent complex refractive indices of the perovskite are measured by ellipsometry as described in Section 2.4. Those for the other materials are taken from the literature (Supplementary Table 3). All the layers except glass are modeled as optically coherent. The drift-diffusion parameters for all materials are reported in Supplementary Table 3. The drift-diffusion model in steady-state mode is solved by letting SETFOS automatically select the appropriate solver (Newton or Gummel) and the corresponding settings for the residuum and damping factors during the computation. The Air Mass 1.5 ASTM G-173-03 (included in the SETFOS database) with 0° incident angle is adopted as the reference spectrum for 1 sun illumination. The solar irradiation on a specific date/time and location is calculated using the SMARTS model implemented in Setfos[103]. Both direct and diffuse solar radiation are considered, assuming illumination of a solar cell parallel to the ground, located in Treviso, Italy (45.65 °N, 12.18 °E, 18 m above sea level) at a user-defined date and time. The total solar radiation is described in terms of global horizontal irradiance, which is the sum of direct and diffuse radiation. Direct radiation is given by the direct normal radiation multiplied by the cosine of the solar zenith angle. Diffuse light is modeled by activating the scattering mode in SETFOS with 30 incident angles from 0 to 90°. A clear-sky scenario is always considered.

RNA extraction, library preparation, sequencing and bioinformatic analyses

For RNA extraction and sequencing, multiple replicates were employed, each consisting of four seedlings within a Magenta™ box. Specifically, three biological replicates were used for plants cultivated under glass (G) conditions, and two for those grown under a perovskite layer (P) to provide comparable biological mass[104]. Shoots (approximately 100 mg of plant material *per* sample) were ground in liquid N_2 in 2-ml tubes filled with two steel beads (diameter 0.4 mm) and homogenized through a TissueLyser II (Qiagen, Valencia, CA, USA) at 28Hz for 60 seconds. Total RNA was isolated by using a CTAB-based method[105]. A list of used reagents for RNA extraction is reported in Supplementary Data 4. The RNA was resuspended in RNase-free water and its quantity was determined by using a Nanodrop 2000 spectrophotometer (Thermo Fisher Scientific, Waltham, MA, USA). Library preparation and RNA sequencing were performed by IGATech located in Udine (Italy). The Universal Plus mRNA-Seq kit (Tecan Genomics, Redwood City, CA) was used for library preparation following the manufacturer's instructions (library type: fr-secondstrand). Libraries were then prepared for sequencing and sequenced on paired-end 150 bp mode on NovaSeq 6000 (Illumina, San Diego, CA). In total, 5 Illumina RNA-seq libraries were generated and sequenced.

The RNA sequencing data were processed through Illumina BCL Convert v3.9.31 to perform the base calling, demultiplexing, and adapter masking processes. Subsequently, ERNE software[106] was employed to trim low-quality bases and adapters. The filtered reads were then aligned on the radicchio reference genome[107] using STAR software[48], which is specifically designed for splice junction mapping in RNA-Seq reads. Transcript assembly and quantification, including the identification of various spliced variants at each gene locus, were performed using Stringtie[108]. For differential expression analysis, the reads overlapping with genes were quantified using htseq-count[109]. The software DESeq2 was then applied to read counts obtained from htseq-count of each gene to model differential expression using a Generalized Linear Model (GLM), enabling the comparison of expression levels across genes and transcripts[110]. The identification of differentially expressed genes (DEGs) was conducted post-normalization of count data and correction for multiple testing by DESeq2[110], using a Wald test. For this analysis, condition G was set as the reference one. Differentially expressed genes were identified using a threshold of an adjusted p-value ≤0.05. Both the identified DEGs and the entire transcriptome of the radicchio genome were annotated via Blast2GO[111] to achieve an updated functional annotation. The dataset (raw data) that supports the findings of this study is available in the NCBI Sequence Read Archive (SRA-NCBI) under BioProject accession number PRJNA1106249.

Reporting summary

Further information on research design is available in the Nature Portfolio Reporting Summary linked to this article.

Data availability

The dataset (raw data) that supports the findings of this study is available in the NCBI Sequence Read Archive (SRA-NCBI) under BioProject accession number PRJNA1106249. All data needed to evaluate the conclusions in the paper are provided in the main text, all other

Source data are provided with this paper. All the input files and data for the simulations reported in this article are freely available on Zenodo (https://zenodo.org/records/14620441). Further analytical and interpretive support are available from the corresponding author upon request. Source data are provided with this paper.

References

1. Meinardi, F., Bruni, F. & Brovelli, S. Luminescent solar concentrators for building-integrated photovoltaics. *Nat. Rev. Mater.* **2**, 1–9 (2017).
2. Richards, B. S. & Howard, I. A. Luminescent solar concentrators for building integrated photovoltaics: opportunities and challenges. *Energy Environ. Sci.* **8** (2023)
3. Lin, H. et al. Silicon heterojunction solar cells with up to 26.81% efficiency achieved by electrically optimized nanocrystalline-silicon hole contact layers. *Nat. Energy* **8**, 789–799 (2023).
4. Cantagallo, J., Medan, D. & Hall, A. Grain number in sunflower as affected by shading during floret growth, anthesis and grain setting. *Field Crops Res.* **85**, 191–202 (2004).
5. Worku, W., Skjelvåg, A. & Gislerød, H. Responses of common bean (phaseolus vulgaris l.) to photosynthetic irradiance levels during three phenological phases. *Agronomie* **24**, 267–274 (2004).
6. Marrou, H., Wéry, J., Dufour, L. & Dupraz, C. Productivity and radiation use efficiency of lettuces grown in the partial shade of photovoltaic panels. *Eur. J. Agron.* **44**, 54–66 (2013).
7. Martinho, F. Challenges for the future of tandem photovoltaics on the path to terawatt levels: a technology review. *Energy Environ. Sci.* **14**, 3840–3871 (2021).
8. Yang, B., Zhang, M., Qiao, G. & Zhang, H. Perovskite solar cells: Emerging photovoltaic technology for achieving net-zero emission agrivoltaics ecosystem. *Sol. RRL* **7**, 2300217 (2023).
9. Valastro, S. et al. Out-of-glovebox integration of recyclable europium-doped cspbi3 in triple-mesoscopic carbon-based solar cells exceeding 9% efficiency. *Sol. RRL* **6**, 2200267 (2022).
10. National Renewable Energy Laboratory. Nrel Charts. https://www.nrel.gov/pv/cell-efficiency.html (2024)
11. Culiik, P. et al. Design and cost analysis of 100 mw perovskite solar panel manufacturing process in different locations. *ACS Energy Lett.* **7**, 3039–3044 (2022).
12. Kokkonen, M. et al. Advanced research trends in dye-sensitized solar cells. *J. Mater. Chem. A* **9**, 10527–10545 (2021).
13. Kweon, K. E. et al. Influence of external conditions on the black-to-yellow phase transition of cspbi3 based on first-principles calculations: pressure and moisture. *Chem. Mater.* **35**, 2321–2329 (2023).
14. Zhu, H. et al. Long-term operating stability in perovskite photovoltaics. *Nat. Rev. Mater.* **8**, 569–586 (2023).
15. Li, J. et al. Biological impact of lead from halide perovskites reveals the risk of introducing a safe threshold. *Nat. Commun.* **11**, 310 (2020).
16. Wang, T. et al. Room temperature nondestructive encapsulation via self-crosslinked fluorosilicone polymer enables damp heat-stable sustainable perovskite solar cells. *Nat. Commun.* **14**, 1342 (2023).
17. Valastro, S. et al. Preventing lead leakage in perovskite solar cells with a sustainable titanium dioxide sponge. *Nat. Sustainability* **6**, 974–983 (2023)
18. Grätzel, M. Mesoscopic solar cells for electricity and hydrogen production from sunlight. *Chem. Lett.* **34**, 8–13 (2005).
19. Friman-Peretz, M. et al. Microclimate and crop performance in a tunnel greenhouse shaded by organic photovoltaic modules–comparison with conventional shaded and unshaded tunnels. *Biosyst. Eng.* **197**, 12–31 (2020).
20. Waller, R., Kacira, M., Magadley, E., Teitel, M. & Yehia, I. Semi-transparent organic photovoltaics applied as greenhouse shade for spring and summer tomato production in arid climate. *Agronomy* **11**, 1152 (2021).
21. Gorjian, S. et al. Progress and challenges of crop production and electricity generation in agrivoltaic systems using semi-transparent photovoltaic technology. *Renew. Sustain. Energy Rev.* **158**, 112126 (2022).
22. Barichello, J. et al. Stable semi-transparent dye-sensitized solar modules and panels for greenhouse application. *Energies* **14**, 6393 (2021).
23. Faheem, M. B. et al. Synergistic approach toward erbium-passivated triple-anion organic-free perovskite solar cells with excellent performance for agrivoltaics application. *ACS Appl. Mater. Interfaces* **14**, 6894–6905 (2022).
24. Smith, H. Phytochromes and light signal perception by plants—an emerging synthesis. *Nature* **407**, 585–591 (2000).
25. Quail, P. H. Photosensory perception and signalling in plant cells: new paradigms? *Curr. Opin. cell Biol.* **14**, 180–188 (2002).
26. Roeber, V. M., Bajaj, I., Rohde, M., Schmülling, T. & Cortleven, A. Light acts as a stressor and influences abiotic and biotic stress responses in plants. *Plant, Cell Environ.* **44**, 645–664 (2021).
27. Kleine, T., Kindgren, P., Benedict, C., Hendrickson, L. & Strand, A. Genome-wide gene expression analysis reveals a critical role for cryptochrome1 in the response of arabidopsis to high irradiance. *Plant Physiol.* **144**, 1391–1406 (2007).
28. Maraveas, C. & Bartzanas, T. Application of internet of things (iot) for optimized greenhouse environments. *AgriEngineering* **3**, 954–970 (2021).
29. Avayu, O., Almeida, E., Prior, Y. & Ellenbogen, T. Composite functional metasurfaces for multispectral achromatic optics. *Nat. Commun.* **8**, 14992 (2017).
30. Semeraro, T. et al. Shading effects in agrivoltaic systems can make the difference in boosting food security in climate change. *Appl. Energy* **358**, 122565 (2024).
31. Laurenčíková, N., Živčák, M., Neugart, S. & Pöhnl, T. Influence of uv radiation-absorbing foils on secondary plant metabolites in three lettuce cultivars (lactuca sativa l. and cichorium intybus l.). *Front. Food Sci. Technol.* **3**, 1208100 (2023).
32. Choi, B. B. et al. Quality and antioxidant properties of sponge cake containing radicchio (cichorium intybus l.) powder. *Korean J. Food Nutr.* **28**, 910–917 (2015).
33. Alekel, D. L. et al. Isoflavone-rich soy protein isolate attenuates bone loss in the lumbar spine of perimenopausal women. *Am. J. Clin. Nutr.* **72**, 844–852 (2000).
34. Xiao, Z., Lester, G. E., Luo, Y. & Wang, Q. Assessment of vitamin and carotenoid concentrations of emerging food products: edible microgreens. *J. Agric. Food Chem.* **60**, 7644–7651 (2012).
35. D'evoli, L. et al. Red chicory (cichorium intybus l. cultivar) as a potential source of antioxidant anthocyanins for intestinal health. *Oxid. Med. Cell. Longev.* **2013** (2013)
36. Bais, H. P. & Ravishankar, G. A. Cichorium intybus l–cultivation, processing, utility, value addition and biotechnology, with an emphasis on current status and future prospects. *J. Sci. Food Agric.* **81**, 467–484 (2001).
37. Rangarajan, A. & Ingall, B. Mulch color affects radicchio quality and yield. *HortScience* **36**, 1240–1243 (2001).
38. Pereira, Bd. J., Cecílio Filho, A. B. & La Scala, N. Greenhouse gas emissions and carbon footprint of collard greens, spinach and chicory production systems in southeast of brazil. *Front. Plant Sci.* **13**, 1015307 (2022).
39. Gardenersworld. How to grow chicory. https://www.gardenersworld.com/how-to/grow-plants/how-to-grow-chicory/ (2024)
40. Zhao, X. et al. Accelerated aging of all-inorganic, interface-stabilized perovskite solar cells. *Science* **377**, 307–310 (2022).

41. Wang, J. et al. 21.15%-efficiency and stable γ-cspbi3 perovskite solar cells enabled by an acyloin ligand. *Adv. Mater.* **35**, 2210223 (2023).
42. Min, H. et al. Perovskite solar cells with atomically coherent interlayers on sno2 electrodes. *Nature* **598**, 444–450 (2021).
43. Bouazizi, S. et al. Methylammonium lead triiodide perovskite-based solar cells efficiency: Insight from experimental and simulation. *J. Mol. Graph. Model.* **122**, 108458 (2023).
44. Chang, Q. et al. Precursor engineering enables high-performance all-inorganic cspbibr2 perovskite solar cells with a record efficiency approaching 13%. *J. Energy Chem.* **90**, 16–22 (2024).
45. Alberti, A. et al. Formation of cspbi3 γ-phase at 80 °C by europium-assisted snowplow effect. *Adv. Energy Sustainability Res.* **2**, 2100091 (2021).
46. Alberti, A. et al. Perovskite solar cells from the viewpoint of innovation and sustainability. *Phys. Chem. Chem. Phys.* **24**, 21549–21566 (2022)
47. Valastro, S. et al. Black-yellow bandgap trade-off during thermal stability tests in low-temperature eu-doped cspbi3. *Sol. RRL* **6**, 2200008 (2022).
48. Dobin, A. et al. Star: ultrafast universal rna-seq aligner. *Bioinformatics* **29**, 15–21 (2013).
49. Stallknecht, E. J. et al. Designing plant–transparent agrivoltaics. *Sci. Rep.* **13**, 1903 (2023).
50. Frouin, R. & Pinker, R. T. Estimating photosynthetically active radiation (par) at the earth's surface from satellite observations. *Remote Sens. Environ.* **51**, 98–107 (1995).
51. Smecca, E. et al. Two-step mapbi 3 deposition by low-vacuum proximity-space-effusion for high-efficiency inverted semi-transparent perovskite solar cells. *J. Mater. Chem. A* **9**, 16456–16469 (2021).
52. Koh, T. M. et al. Halide perovskite solar cells for building integrated photovoltaics: transforming building façades into power generators. *Adv. Mater.* **34**, 2104661 (2022).
53. Zhang, Z. et al. Towards low-temperature processing of efficient γ-cspbi 3 perovskite solar cells. *J. Mater. Chem. A* **11**, 16115–16126 (2023).
54. Heinze, K. L., Wessel, P., Mauer, M., Scheer, R. & Pistor, P. Stoichiometry dependent phase evolution of co-evaporated formamidinium and cesium lead halide thin films. *Mater. Adv.* **3**, 8695–8704 (2022).
55. Alberti, A. et al. Hybrid perovskites for photovoltaics: Story, challenges and opportunities. *La Riv. Nuovo Cim.* **42**, 301–366 (2019).
56. La Magna, P. et al. X-ray investigation of cspbi3: Eucl3 infiltrated into gig-lox tio2 spongy layers for perovskite solar cells applications. *Nanomaterials* **13**, 2910 (2023).
57. Valastro, S. et al. Optical behaviour of γ-black cspbi3 phases formed by quenching from 80 °C and 325 °C. *J. Phys.: Mater.* **4**, 034011 (2021).
58. Spampinato, C. et al. Infiltration of cspbi3: Eui2 perovskites into tio2 spongy layers deposited by gig-lox sputtering processes. *Solar* **3**, 347–361 (2023).
59. Ummadisingu, A., Meloni, S., Mattoni, A., Tress, W. & Grätzel, M. Crystal-size-induced band gap tuning in perovskite films. *Angew. Chem. Int. Ed.* **60**, 21368–21376 (2021).
60. Stapleton, A. E. Ultraviolet radiation and plants: burning questions. *Plant Cell* **4**, 1353 (1992).
61. Tang, B. et al. High stability and temperature-dependent photoluminescence of orthorhombic cspbi3 perovskite nanoparticles. *Adv. Opt. Mater.* **8**, 2000498 (2020).
62. Liu, F. et al. Highly luminescent phase-stable cspbi3 perovskite quantum dots achieving near 100% absolute photoluminescence quantum yield. *ACS Nano* **11**, 10373–10383 (2017).
63. Gau, D. L., Galain, I., Aguiar, I. & Marotti, R. E. Origin of photoluminescence and experimental determination of exciton binding energy, exciton-phonon interaction, and urbach energy in γ-cspbi3 nanoparticles. *J. Lumin.* **257**, 119765 (2023).
64. Hogewoning, S. W. et al. Blue light dose–responses of leaf photosynthesis, morphology, and chemical composition of cucumis sativus grown under different combinations of red and blue light. *J. Exp. Bot.* **61**, 3107–3117 (2010).
65. National Renewable Energy Laboratory. Nrel PVwatts chart.. https://pvwatts.nrel.gov/pvwatts.php (2024)
66. Kirakosyan, R. N. et al. Influence of plant growth regulators and artificial light on the growth and accumulation of inulin of dedifferentiated chicory (cichorium intybus l.) callus cells. *Life* **12**, 1524 (2022).
67. Shibaeva, T. G. et al. Effects of extended light/dark cycles on solanaceae plants. *Plants* **13**, 244 (2024).
68. Zhang, X. et al. Inorganic cspbi3 perovskite coating on pbs quantum dot for highly efficient and stable infrared light converting solar cells. *Adv. Energy Mater.* **8**, 1702049 (2018).
69. Liang, L. et al. Optical management with nanoparticles for a light conversion efficiency enhancement in inorganic γ-cspbi3 solar cells. *Nano Lett.* **19**, 1796–1804 (2019).
70. Faust, J. E., Holcombe, V., Rajapakse, N. C. & Layne, D. R. The effect of daily light integral on bedding plant growth and flowering. *HortScience* **40**, 645–649 (2005).
71. Gao, W., He, D., Ji, F., Zhang, S. & Zheng, J. Effects of daily light integral and led spectrum on growth and nutritional quality of hydroponic spinach. *Agronomy* **10**, 1082 (2020).
72. Kathare, P. K. & Huq, E. Light-regulated pre-mrna splicing in plants. *Curr. Opin. Plant Biol.* **63**, 102037 (2021).
73. Behn, H. et al. Uv-b transmittance of greenhouse covering materials affects growth and flavonoid content of lettuce seedlings. *Eur. J. Hortic. Sci.* **75**, 259 (2010).
74. Jenkins, G. I. Signal transduction in responses to uv-b radiation. *Annu. Rev. Plant Biol.* **60**, 407–431 (2009).
75. Hernández, R. & Kubota, C. Physiological responses of cucumber seedlings under different blue and red photon flux ratios using leds. *Environ. Exp. Bot.* **121**, 66–74 (2016).
76. Wang, J., Lu, W., Tong, Y. & Yang, Q. Leaf morphology, photosynthetic performance, chlorophyll fluorescence, stomatal development of lettuce (lactuca sativa l.) exposed to different ratios of red light to blue light. *Front. Plant Sci.* **7**, 250 (2016).
77. Runkle, E. S. & Heins, R. D. Specific functions of red, far red, and blue light in flowering and stem extension of long-day plants. *J. Am. Soc. Horticultural Sci.* **126**, 275–282 (2001).
78. Malumbres, M. & Pellicer, A. Ras pathways to cell cycle control and cell transformation. *Front. Biosci.* **3**, 887–912 (1998).
79. Rojas, A. M., Fuentes, G., Rausell, A. & Valencia, A. The ras protein superfamily: evolutionary tree and role of conserved amino acids. *J. Cell Biol.* **196**, 189–201 (2012).
80. Hála, M., Soukupová, H., Synek, L. & Žárskỳ, V. Arabidopsis rab geranylgeranyl transferase β-subunit mutant is constitutively photomorphogenic, and has shoot growth and gravitropic defects. *Plant J.* **62**, 615–627 (2010).
81. Li, Q. et al. Comparative transcriptome analysis revealed differential gene expression involved in wheat leaf senescence between stay-green and non-stay-green cultivars. *Front. Plant Sci.* **13**, 971927 (2022).
82. Xu, Y. & Crouch, J. H. Marker-assisted selection in plant breeding: From publications to practice. *Crop Sci.* **48**, 391–407 (2008).
83. Zhang, M. et al. The arabidopsis u-box e3 ubiquitin ligase pub30 negatively regulates salt tolerance by facilitating bri1 kinase inhibitor 1 (bki1) degradation. *Plant. Cell Environ.* **40**, 2831–2843 (2017).

84. Ding, L. et al. Aquaporin pip2; 1 affects water transport and root growth in rice (oryza sativa l.). *Plant Physiol. Biochem.* **139**, 152–160 (2019).
85. Harari-Steinberg, O., Ohad, I. & Chamovitz, D. A. Dissection of the light signal transduction pathways regulating the two early light-induced protein genes in arabidopsis. *Plant Physiol.* **127**, 986–997 (2001).
86. Heddad, M. et al. Differential expression and localization of early light-induced proteins in arabidopsis. *Plant Physiol.* **142**, 75–87 (2006).
87. Morris, W. L. et al. Utilisation of the mva pathway to produce elevated levels of the sesquiterpene α-copaene in potato tubers. *Phytochemistry* **72**, 2288–2293 (2011).
88. Bett, A. J. et al. Semi-transparent perovskite solar cells with ito directly sputtered on spiro-ometad for tandem applications. *ACS Appl. Mater. interfaces* **11**, 45796–45804 (2019).
89. Wang, Y. et al. Encapsulation and stability testing of perovskite solar cells for real life applications. *ACS Mater. Au* **2**, 215–236 (2022).
90. Magliano, E. et al. Semitransparent perovskite solar cells with ultrathin protective buffer layers. *ACS Appl. Energy Mater.* **6**, 10340–10353 (2023).
91. Bisconti, F. et al. Managing transparency through polymer/perovskite blending: a route toward thermostable and highly efficient, semi-transparent solar cells. *Nano Energy* **89**, 106406 (2021).
92. Campana, P. E., Stridh, B., Amaducci, S. & Colauzzi, M. Optimisation of vertically mounted agrivoltaic systems. *J. Clean. Prod.* **325**, 129091 (2021).
93. Paris, B. et al. Energy use in greenhouses in the EU: a review recommending energy efficiency measures and renewable energy sources adoption. *Appl. Sci.* **12**, 5150 (2022).
94. Jena, A. K., Kulkarni, A., Sanehira, Y., Ikegami, M. & Miyasaka, T. Stabilization of α-cspbi3 in ambient room temperature conditions by incorporating eu into cspbi3. *Chem. Mater.* **30**, 6668–6674 (2018).
95. Spampinato, C. et al. Spongy TiO_2 layers deposited by gig-lox sputtering processes: contact angle measurements. *J. Vac. Sci. Technol. B* **41**, 012802 (2023).
96. Arena, V. et al. Lead detection in a gig-lox tio2 sponge by x-ray reflectivity. *Nanomaterials* **13**, 1397 (2023).
97. Tauc, J., Menth, A. & Wood, D. Optical and magnetic investigations of the localized states in semiconducting glasses. *Phys. Rev. Lett.* **25**, 749 (1970).
98. Jellison Jr, G. & Modine, F. Erratum:"parameterization of the optical functions of amorphous materials in the interband region"[appl. phys. lett. 69, 371 (1996)]. *Appl. Phys. Lett.* **69**, 2137–2137 (1996).
99. Capper, P., Willoughby, A. & Kasap, S. O. *Optical Properties of Materials and Their Applications* (John Wiley & Sons, 2020)
100. Mannino, G. et al. Temperature-dependent optical band gap in cspbbr3, mapbbr3, and fapbbr3 single crystals. *J. Phys. Chem. Lett.* **11**, 2490–2496 (2020).
101. Mannino, G. et al. $CsPbBr_3$, $MAPbBr_3$, and $FAPbBr_3$ bromide perovskite single crystals: interband critical points under dry N_2 and optical degradation under humid air. *J. Phys. Chem. C* **125**, 4938–4945 (2021).
102. Fluxim AG, S. Setfos (Semiconducting thin film optics simulator); version 5.4.12. https://www.fluxim.com/setfos-intro (2024)
103. Gueymard, C. A. The smarts spectral irradiance model after 25 years: New developments and validation of reference spectra. *Sol. Energy* **187**, 233–253 (2019).
104. Schurch, N. J. et al. How many biological replicates are needed in an rna-seq experiment and which differential expression tool should you use? *Rna* **22**, 839–851 (2016).
105. Chang, S., Puryear, J. & Cairney, J. A simple and efficient method for isolating rna from pine trees. *Plant Mol. Biol. Rep.* **11**, 113–116 (1994).
106. Del Fabbro, C., Scalabrin, S., Morgante, M. & Giorgi, F. M. An extensive evaluation of read trimming effects on illumina ngs data analysis. *PLoS ONE* **8**, 85024 (2013).
107. Fan, W. et al. The genomes of chicory, endive, great burdock and yacon provide insights into asteraceae palaeo-polyploidization history and plant inulin production. *Mol. Ecol. Resour.* **22**, 3124–3140 (2022).
108. Pertea, M. et al. Stringtie enables improved reconstruction of a transcriptome from rna-seq reads. *Nat. Biotechnol.* **33**, 290–295 (2015).
109. Anders, S. & Huber, W. Differential expression analysis for sequence count data. *Genome Biol.* **11**, R106 (2010)
110. Love, M., Anders, S. & Huber, W. Differential analysis of count data–the deseq2 package. *Genome Biol.* **15**, 10–1186 (2014).
111. Conesa, A. et al. Blast2go: a universal tool for annotation, visualization and analysis in functional genomics research. *Bioinformatics* **21**, 3674–3676 (2005).

Acknowledgements

The work was supported by the CNR-funded project Vertigrow, CUP B15F21004410005. The authors also wish to thank FSE (Fondo Sociale Europeo) and the "Programma Operativo Nazionale" (PON) for Sicily 2014-2020). This work was partially supported by the European Union (NextGeneration EU), through the MUR-PNRR project SAMOTHRACE - Sicilian MicronanoTech Research and Innovation Center (ECS00000022, CUP B63C22000620005). The authors also thank Sebastian Ferranti (CNR-IMM) for his technical support.

Author contributions

Conceptualization, A.A., R.B., C.S., S.V.; methodology, C.S., S.V., G.C., F.S.; validation, A.A., R.B., A.L.M.; formal analysis, C.S., S.V., E.S., V.A, G.M., F.S., G.C., L.C.; Software, G.C., A.L.M.; investigation, C.S., S.V., F.S.; resources, R.B., A.A., G.M., A.L.M.; data curation, C.S., S.V., F.S.; writing—original draft preparation, C.S., S.V., G.C.; writing—review and editing, A.A., R.B., G.M., A.L.M.; supervision, R.B., A.A.; project administration, R.B., A.A.; funding acquisition, R.B., A.A. All authors have read and agreed to the published version of the manuscript.

Competing interests

The authors declare no competing interests.

Additional information

Supplementary information The online version contains supplementary material available at https://doi.org/10.1038/s41467-025-56227-9.

Correspondence and requests for materials should be addressed to Salvatore Valastro, Raffaella Balestrini or Alessandra Alberti.

Peer review information *Nature Communications* thanks Hong Zhang, Xiaofan Na, and the other, anonymous, reviewer(s) for their contribution to the peer review of this work. A peer review file is available.